Solar Energy Advances 1 (2021) 100003

Contents lists available at ScienceDirect

Solar Energy Advances

journal homepage: www.elsevier.com/locate/seja

Sinusoidal small-signal (AC) and steady-state (DC) analysis of large-area solar cells

Ennio Luigi Comi [a,*], Evelyne Knapp [a], Stefano Weidmann [b], Christoph Kirsch [a], Sandra Jenatsch [b], Roman Hiestand [b], Beat Ruhstaller [a,b]

[a] Institute of Computational Physics, Zurich University of Applied Sciences, Wildbachstr. 21, 8401, Winterthur, Switzerland
[b] Fluxim AG, Katharina-Sulzer-Platz 2, 8406 Winterthur, Switzerland

ARTICLE INFO

Keywords:
Electrochemical impedance spectroscopy (EIS)
Large-area device simulation
Silicon solar cells
Finite element method (FEM)
Device characterization

ABSTRACT

Beside fabrication challenges, efficiency loss factors of solar cells such as shunts and an increasing series resistance caused by the sheet resistance of the electrodes, are issues to be tackled when scaling novel photovoltaic devices up from laboratory to industrial size. We present a FEM (Finite Element Method) software that supports the upscaling process from small- to large-area devices. Considering Ohm's law in the top and bottom electrodes, which are coupled by a vertical current, the software solves for the electric potential distribution in the 2D electrode domains. In addition to steady-state simulations, we introduce a small-signal analysis that allows us to compute the influence of resistive electrodes and defects on the frequency-dependent impedance response. Herein, we describe the implemented numerical model for the AC (alternating current) mode. The steady-state model was validated with measurements using monocrystalline silicon solar cells of several sizes and one cell was intentionally shunted with a laser to demonstrate the fingerprints of these defects in the DC (direct current) and AC response. In a further step, we verify the numerical simulation of the AC model with an analytical solution to a one-dimensional AC model for a simplistic quadratic domain and linearized coupling law. Overall, the presented AC model is able to reproduce and predict the behavior of the measurements of the original and later shunted silicon solar cell. Thereby we have demonstrated that the presented AC model is a powerful tool to study devices in the frequency domain which complements characterization in steady-state.

1. Introduction

During the past decade, purely economic reasons have started to drive the photovoltaic market rendering government subsidies superfluous. The continuing decline in investment costs for solar energy is leading to a lower levelized cost of electricity, which is already competitive and predicted to significantly underprice conventional energy sources in the near future [1].

Although efficient and inexpensive homojunction silicon solar cells dominate the market, third-generation photovoltaics, such as perovskite and monolithic perovskite/Si tandem cells, have made enormous progress in terms of power conversion efficiency (PCE) in a very short period of time. While the certified PCE of lab-scale single junction perovskite solar cells impressively reached 25.5 %, tandem cells with 29.1 % efficiency have already exceeded the efficiency record of 26.7 % for heterojunction Si-cells [2,3].

Unfortunately, the reported efficiencies have only been achieved with cells on laboratory scale, typically < 1 cm^2 [4–8]. To become commercially competitive with well-established solar cell technologies, the upscaling from small-area to large-area third-generation devices is an essential and challenging requirement. Zheng et al. made considerable progress with large-area perovskite/homojunction-Si tandem cells, reporting PCEs of 23 % on 4 cm^2 and 21.8 % on 16 cm^2 [9–11]. Nevertheless, a novel device with an active area of 16 cm^2 is still 14.5 times smaller compared to a commercially available 6″ silicon wafer.

In addition to stability issues [12] and the challenges concerning the fully scalable device layer fabrication of novel devices [13], upscaling also inevitably entails efficiency losses due to an increase in series resistance, more likely occurring shunts and substrate heating [14]. The higher series resistance is mainly caused by the longer travel distance of charge carriers through the transparent conductive oxide (TCO), which is affected by the sheet resistance (R_{sh}). This is reflected in a lower fill factor (FF) and short circuit current (J_{sc}) [14,15]. Nevertheless, high sheet resistances in silicon solar cells have led to an improvement in V_{oc} and J_{sc}, due to lower emitter recombination losses and optical effects such as a better short wavelength response [16–19].

In order to reduce the influence of the sheet resistance on a cell's series resistance, screen printed front metallization grids are used in

* Corresponding author.
E-mail address: comi@zhaw.ch (E.L. Comi).

https://doi.org/10.1016/j.seja.2021.100003
Received 4 March 2021; Received in revised form 21 September 2021; Accepted 21 September 2021
Available online 9 October 2021

most commercially available silicon solar cells. More and more large-area third generation devices are produced with optimized metal grids in such a way that maximal efficiency is achieved despite the shading losses [9,10]. A recent study has shown that an advancement of the TCO becomes almost irrelevant when front metal gridlines are applied on perovskite solar cells [20]. In addition, success has also been reported in low-temperature screen printed metallization of novel devices, which is a further step towards commercialization compared to evaporated metallization [21].

The software Laoss [22–26] (Large-Area Organic Semiconductor Simulation) presented here supports the process of upscaling from small-area cells to large-area devices and the optimization of metal gridlines with a 2D FEM solver, solving Ohm's law on the top and bottom electrode. The electrodes are coupled with a 1D current-voltage-law of a quasi-ideal device in vertical direction, leading to a 2D + 1D structure. This modelling method reduces computation time by a considerable amount compared to a full 3D simulation due to the reduced amount of degrees of freedom.

The vertical charge carrier flow in the semiconductor stack is mainly caused by a homogeneous electric field between top and bottom electrode. For thin-film devices e.g. perovskite or organic solar cells, the electric field is further enhanced by the small electrode spacing and in some cases also by larger band gaps [27]. Therefore, Laoss is especially suited for thin-film devices and saves computation time with the presented 2D + 1D approach. The assumption of a vertical current flow is also justified for classical silicon solar cells with an aluminium back-surface field (Al-BSF), passivated emitter and rear (PERC) and passivated emitter and totally diffused rear (PERT) cells [28–30]. For passivated emitter with locally diffused rear (PERL) cells, we can assume a predominantly vertical current flow for the major part of the stack, but it would cause an additional modelling effort to compensate for the oblique current crowding at the local rear contacts [31]. Our software tool reaches its limits when integrated back contact (IBC) devices are simulated, where the charge carriers flow generally lateral [28,32]. Simulations of IBC cells have been carried out with quasi-3D cross connected electrical networks using the software SPICE [33] or with full 3D cell models using Quokka [34,35] for instance. Higher dimensions and better spacial resolutions are often accompanied with more time-consuming calculations. However, these alternative simulation methods are applicable to general device types and can also help analysing EL and PL images [36] or optimizing the back contact design, as shown by Renshaw et al. using the multidimensional software Sentaurus Device [37].

Laoss has recently been extended to the frequency domain for sinusoidal small-signal analysis. The AC mode aims to compute the influence of non-ideal electrodes on electrochemical impedance spectroscopy (EIS) data. EIS is a non-destructive measurement technique, which is usually performed on small cells and widely used to analyse charge transport processes, doping densities and recombination mechanisms but also properties of interfaces and contacts from several types of photovoltaic devices [38–43]. Herein, we describe the steady-state and time harmonic models of our software's electrical module. We demonstrate how this FEM solver is able to model non-ideal electrodes and we present numerical simulation results in steady-state and frequency domains. The fact that different sizes of novel devices are difficult to manufacture consistently and reliably makes a validation with this type of cells very difficult. Therefore, we have laser-cut monocrystalline silicon solar cells into different sizes and shunted one device intentionally. We consequently validate the simulation results by a comparison with measurements of these devices.

2. Methodology

For an electric current to flow in a large-area semiconductor device, charge carriers in general must travel vertically through the layer stack and laterally through the electrodes to the contacts. The charge carrier transport via the electrodes is hampered by ohmic losses due to the sheet resistance of the conducting top and bottom layer [44], which our software quantifies using 2D domains. The local one-dimensional coupling law connects the 2D electrodes and describes the physical characteristics of semiconductor devices such as OLEDs and solar cells. This setup allows to study and optimize the influence of non-ideal electrodes on the performance of solar cells and OLEDs [22]. Fig. 1 depicts the basic modelling setup of Laoss with 2D top and bottom domains, connected by a local 1D coupling law.

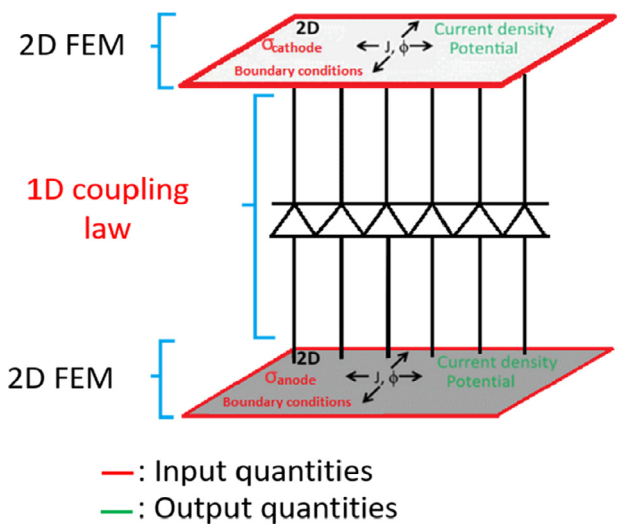

Fig. 1. Schematic structure of the electrical model of the Laoss software with the coupled 2D domains and a 1D coupling law.

Kirsch et al. [23] presented Laoss' electrothermal model, assuming a constant electric potential of 0 V and a constant temperature of 300 K in the bottom electrode, leading to remaining 2D equations in the top electrode. Here we briefly introduce the electrical steady-state model and additionally its linearization for the AC response.

2.1. Electrical steady-state model

The mathematical steady-state model for electrical simulations is based on Ohm's law for the electrode domains in a differential form for the current density J and the electric field E (equation (1))

$$J = \sigma E \quad \text{with} \quad E = -\nabla U. \tag{1}$$

The electric scalar potential in 3D is denoted as U and σ is the specific conductivity of the electrode material.

This 3D model is then reduced to a 2D + 1D model by the assumption that the current flux is predominately vertical in the semiconductor device stack and by averaging the potential in vertical direction inside the electrodes. Consequently, with the potential distribution in 2D denoted as φ, these simplifications lead to the following two current continuity equations for the top (equation (2)) and bottom electrode domain (equation (3))

$$-\nabla \cdot \left(R_{\mathrm{sh}}^{\mathrm{T}\,-1} \nabla \varphi^{\mathrm{T}} \right) = j(\varphi^{\mathrm{T}} - \varphi^{\mathrm{B}}) \tag{2}$$

$$-\nabla \cdot \left(R_{\mathrm{sh}}^{\mathrm{B}\,-1} \nabla \varphi^{\mathrm{B}} \right) = -j(\varphi^{\mathrm{T}} - \varphi^{\mathrm{B}}). \tag{3}$$

The left sides of the equations (2) and (3) contain the divergence of the 2D electrode current, which is expressed with Ohm's law from equation (1) and the electric potentials φ^{T} for the top and φ^{B} for the bottom electrode. The right hand sides describe the vertical 1D current density coupling law representing the semiconductor stack between the top and bottom electrode. In the electrical steady-state case, the 1D coupling law can be an analytical expression (e.g. diode model) or also a current-voltage measurement, which describes the physical properties

of a cell which is not affected by area effects. The sheet resistance of the top and bottom electrode, represented as $R_{sh}^{T,B}$, is calculated with the specific conductivity and the thickness of the electrodes.

The 2D + 1D coupled continuity equations (2) and (3) have to be completed with boundary conditions at the top and bottom electrode to obtain a well-posed problem. The software offers a range of boundary conditions to choose from (Dirichlet, Neumann). For the present study we use the default zero-flux Neumann conditions at the boundary of the unconnected edges and Dirichlet conditions at the contacted edges of the domain with a fixed prescribed voltage. This model is then discretized with the Galerkin finite element method with linear shape functions. The top and bottom domains are meshed into triangular elements, which leads to a system of non-linear equations for the unknown local potential [23].

2.2. Electrical AC model

Our FEM software Laoss has recently been extended with a frequency domain solver. As in an impedance spectroscopy measurement, it aims to calculate the impedance $Z(\omega, \varphi)$ for time-harmonic small-signal excitations at different frequencies and bias voltages. This allows to study the influence of non-ideal electrodes in frequency domain by computing the electric potential when the electrodes are excited with a superimposed sinusoidal voltage. The small-signal approach allows us to calculate the impedance for small-signals by linearization [45]. The mathematical model of the frequency domain solver is based on Maxwell's Ampre law in frequency domain

$$\nabla \times H = J + i\omega\bar{\varepsilon}E \tag{4}$$

with the magnetic field strength H, the electric field E, $\omega = 2\pi f$ and $\bar{\varepsilon}$ being the complex permittivity, which is expressed by $\bar{\varepsilon} = \varepsilon_{re} - i\varepsilon_{im}$. The divergence of a curl is zero, therefore equation (4) can be written as

$$0 = \nabla \cdot (J + i\omega\bar{\varepsilon}E) \tag{5}$$

Together with Ohm's law (equation (1)) and with the effective conductivity $\sigma_{eff} = \sigma + \omega\varepsilon_{im}$, one can write

$$0 = \nabla \cdot \left(\left(\sigma_{eff} + i\omega\varepsilon_{re}\right)\nabla U\right). \tag{6}$$

We make use of electro-quasistatic approximation for typical device parameters and the necessary frequency range [46]. We assume

$$||\nabla U|| \gg ||\frac{\partial A}{\partial t}|| \tag{7}$$

where A denotes the magnetic vector potential. Therefore,

$$E = -\nabla U - \frac{\partial A}{\partial t} \tag{8}$$

can be approximated by $E = -\nabla U$. This model in the frequency domain can be reduced to 2D + 1D, similar as in the steady-state model. To reduce the three dimensions, equation (6) is averaged along the thin vertical dimension of the electrode with each electrode having a thickness l. It is assumed that the permittivity and conductivity are independent of the electrode thickness. At this point the sheet resistance R_{sh} is introduced as

$$R_{sh} = \frac{1}{\sigma_{eff} l}. \tag{9}$$

As explained in [46] the permittivity ε_{re} and the resulting sheet elastance gain importance for the result in the optical frequency range or above, but in this regime the electro-quasistatic approximation (equation (7)) does not hold anymore. Therefore, the sheet elastance can be neglected in this case.

With the sheet resistance R_{sh}, the stack current j (coupling law) and the potential distribution U, which is now reduced to 2D as well as the divergence operator, the current conservation equation (6) turns into equation (10) and (11) for the top and bottom electrode, respectively.

$$-\nabla \cdot \left(R_{sh}^{T\,-1}\nabla\varphi\right) = j \text{ and} \tag{10}$$

$$-\nabla \cdot \left(R_{sh}^{B\,-1}\nabla\varphi\right) = -j. \tag{11}$$

In order to use the superposition $\varphi^{T,B} = \varphi_{bias}^{T,B} + \varphi_{AC}^{T,B}e^{i\omega t}$ for the small-signal approximation, with φ_{AC} as the amplitude of the sinusoidal voltage, the stack current has to be linearised around the operating points φ_{bias}^{T} and φ_{bias}^{B}. The superposition of the bias and AC voltage leads to two boundary value problems (BVP) that depend on the potential difference between the top and bottom electrode. One BVP is for the real valued steady-state part and the other one for the complex valued small-signal part. For the time-harmonic part the frequency and bias voltage dependent admittance $Y(\omega, \varphi_{bias})$ is introduced, which is an input parameter determining the coupling law for the AC model.

For the steady-state calculation on the top (equation (12)) and bottom electrode domain (equation (13)) the following holds:

$$-\nabla \cdot \left(R_{sh}^{T\,-1}\nabla\varphi_{bias}^{T}\right) = j(\varphi_{bias}^{T} - \varphi_{bias}^{B}) \tag{12}$$

$$-\nabla \cdot \left(R_{sh}^{B\,-1}\nabla\varphi_{bias}^{B}\right) = -j(\varphi_{bias}^{T} - \varphi_{bias}^{B}). \tag{13}$$

The equations for the calculation of the AC part on the top (equation (14)) and bottom electrode (equation (15)) are:

$$-\nabla \cdot \left(R_{sh}^{T\,-1}\nabla(\varphi_{AC}^{T}e^{i\omega t})\right) = Y(\omega, \varphi_{bias}^{T})(\varphi_{AC}^{T} - \varphi_{AC}^{B}) \tag{14}$$

$$-\nabla \cdot \left(R_{sh}^{B\,-1}\nabla(\varphi_{AC}^{B}e^{i\omega t})\right) = -Y(\omega, \varphi_{bias}^{B})(\varphi_{AC}^{T} - \varphi_{AC}^{B}). \tag{15}$$

The Dirichlet boundary conditions with a prescribed voltage for φ_{bias}^{T}, φ_{bias}^{B}, $\varphi_{AC}^{T}e^{i\omega t}$ and $\varphi_{AC}^{B}e^{i\omega t}$ are applied on the edges of the domain with electrical contacts. Homogeneous Neumann conditions are applied on the remaining edges.

Since the BVPs are just coupled in the vertical direction, the steady-state problem has to be solved first to provide the operating voltage points needed for the linearisation of the AC problem. This BVP indicates that in order to run simulations in the frequency domain, it is necessary to provide two 1D coupling laws of the stack in total. Firstly, a current-voltage characteristic j has to be imported to calculate the steady-state solution. Secondly, a frequency and bias voltage dependent impedance law $Y(\omega, \varphi_{bias})$ of the stack is needed. In a measurement, EIS is normally conducted at a certain bias voltage. However, the potential on a large-area electrode drops, due to the sheet resistance, leading to a lower potential and thus to a different admittance $Y(\omega, \varphi_{bias})$ at different locations on the large-area electrode. Therefore, frequency dependent impedance data at different bias voltages have to be provided in order to assess the influence of the potential drop and the sheet resistance on the simulation result.

2.3. Experimental methods

The all-in-one measurement platform Paios [40,47,48] from Fluxim AG has been used to perform impedance spectroscopy and current-voltage measurements of the solar cells. All the measurements have been carried out in the dark. The current-voltage measurements were performed with a starting voltage of -0.2 V and sequential steps to an ending voltage of 0.7 V. A total of 100 steps has been taken with a measurement and settling time of 10 ms for the silicon solar cells. EIS measurements were performed in the dark with a harmonic voltage amplitude of 0.05 V and at 50 frequency points between 5 Hz and 1 MHz. The Al-BSF Motech XS156B3-200R 6″ monocrystalline silicon solar cells were laser cut into 4 cm^2, 9 cm^2 and 25 cm^2 cells. To prevent shunts induced by laser cutting, the edges were gently sanded with fine sandpaper. Afterwards contacts have been soldered on manually with commercially used busbars. TLM (Transmission Line Method) measurements revealed a sheet resistance of 94 Ω/sq. The 4 cm^2 cell was intentionally shunted after a first set of measurements by passing the laser several times over the same spot.

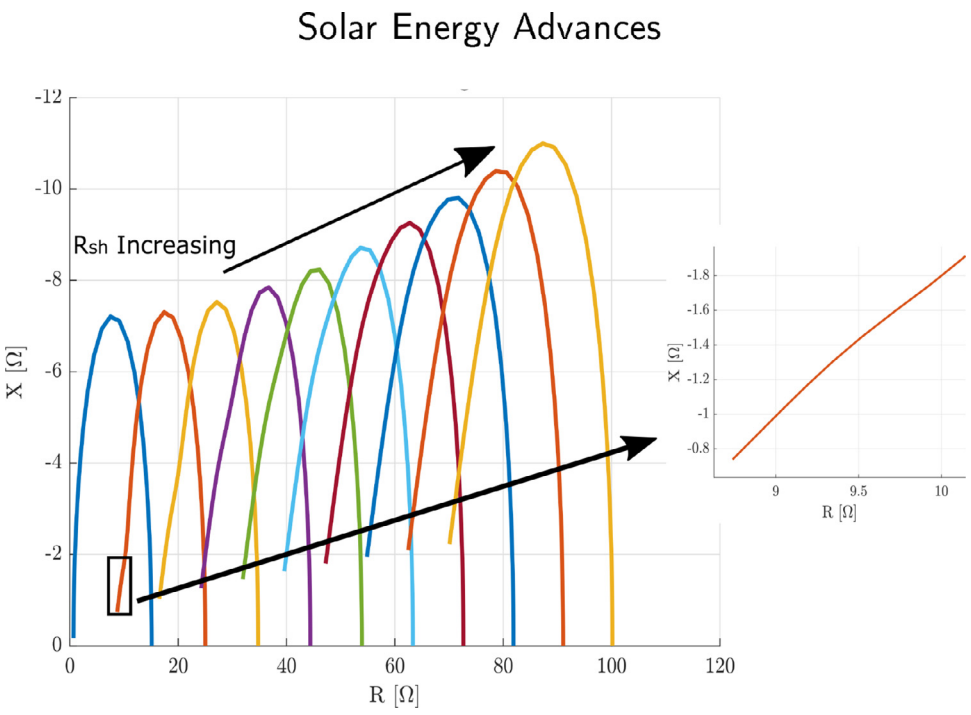

Fig. 2. FEM simulation result represented in a Nyquist plot with simultaneously increasing sheet resistance on the top and bottom electrode from 1 to 136 Ω/sq.

3. Results

3.1. AC-mode verification

In this section we explain and verify the influence of the sheet resistance on the simulated impedance spectra. We discuss the simulated impedance arcs in Fig. 2 and we explain them with equivalent circuits and with an analytical model of a simplistic quadratic electrode domain. Fig. 2 depicts the result of a Laoss AC simulation of a 1.44 cm^2 domain in a Nyquist representation with a bias voltage independent 1D impedance coupling law. We notice that with simultaneously increasing the sheet resistance from 1 to 136 Ω/sq on the top and bottom electrode, the impedance arcs shift towards higher values on the x-axis due to the growing contribution of the sheet resistance to the series resistance and we observe a linear, ≈ 45° inclined high-frequency limit (see Fig. 2). Furthermore, we also observe that the imaginary part is influenced by the sheet resistance and therefore the impedance arcs are inflating with increasing sheet resistance. It is important to note that even with a more realistic choice of the bottom sheet resistance, i.e. with a high conductivity, the simulated impedance arcs would inflate in a similar manner. The impedance arc inflation was not anticipated.

To verify the AC model and to understand the origin of the simulation results obtained from the sheet resistance variation, we start with a simple equivalent circuit model containing a parallel connection of two RC elements and sheet resistances, symbolized by resistors, on the top and bottom side (s. Fig. 3A). The frequency response of this simple circuit in Fig. 3B shows a horizontal shift but no inflation of the arcs when the top and bottom resistances are swept simultaneously. This becomes visible when the analytical impedance expression of this circuit

$$Z = \frac{(R_B + i\omega RC \cdot R_B + R) \cdot (R_T + i\omega RC \cdot R_T + R)}{(1 + i\omega RC) \cdot (R_T + i\omega RC \cdot R_T + 2R + R_B + i\omega RC \cdot R_B)} \tag{16}$$

is simplified with

$$R_T = R_B = R_{TB} \rightarrow Z = \frac{1}{2} \cdot \left(R_{TB} + \frac{R}{1 + i\omega RC} \right) \tag{17}$$

as R_{TB} separates itself from the imaginary part, explaining the horizontal shift of the arcs in Fig. 3B. In order to mimic the inflation of the arcs, we have extended the circuit by one more RC element (Fig. 3C). It attempts to symbolize a small 1D segment of the time-harmonic FEM model implemented in Laoss. The frequency response of this equivalent circuit shown in Fig. 3D with simultaneously swept resistances on the top and bottom electrodes exhibits similar tendencies with the inflation of the impedance arcs as the FEM simulation shown above in Fig. 2. The horizontal shift is caused by the top and bottom resistance, which after the simplification of the circuit form a resistive element in series as can be seen in equation (17). The inflation of the semicircles originates from the influence of the sheet resistance on the imaginary part of the top and bottom resistances.

Even though the equivalent circuit results (Fig. 3D) look similar to the FEM results (Fig. 2), there are clear differences. Firstly, no linear high-frequency limit is observed due to the lack of a constant phase element. Secondly, the peaks of the impedance arcs grow in a different manner. The equivalent circuit models illustrate the influence of the sheet resistance from the bottom and top electrode on the total impedance to some extent. We state that the arcs can no longer be interpreted as in small cells (transport and recombination resistance, see e.g. [49,50]) as the interplay with the sheet resistance on large-area electrodes cannot be easily separated. The sheet resistance affects position, size and shape of the arcs.

As an alternative modelling approach, in the following, we reproduce the FEM simulation results (Fig. 2) with an analytical model of a simple symmetric 1D domain. In a previous publication Lanz et al. [51] we developed a similar analytical model for an illuminated solar cell in steady-state.

We assume identical quadratic domains on the top and bottom electrode with side length L and an identical sheet resistance R_{sh} on both electrodes. The boundary conditions are chosen such that the problem can be treated in one dimension and all derivatives in y-direction vanish. The impedance is computed by integrating the potential difference along the x-axis, which results in the following analytical impedance expression for this simplistic domain

$$Z = \frac{V_{bias}}{LY(\omega) \int_0^L \left(\varphi^T - \varphi^B\right) dx} = \frac{R_{sh}\left(2\coth\left(\frac{kL}{2}\right) + kL\right)}{2kL} \tag{18}$$

Solar Energy Advances

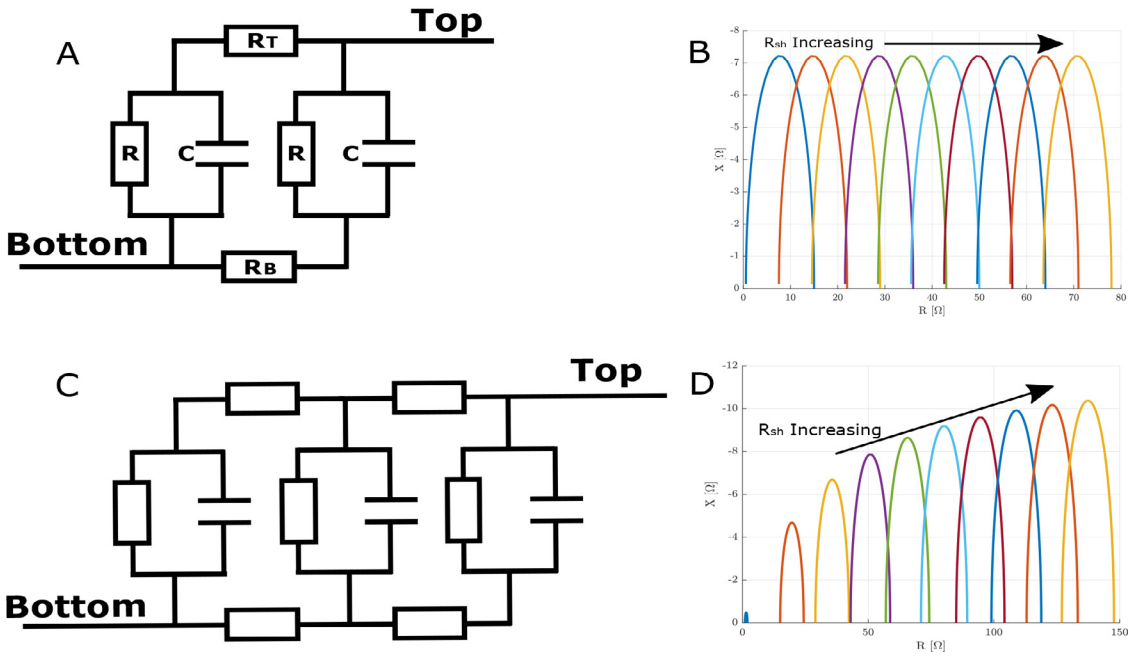

Fig. 3. Equivalent circuit model with top and bottom resistances coupled with two RC elements (A) and three RC elements (C). The resulting impedance spectra of equivalent circuit A with swept top and bottom resistance from 1 to 127 Ω is shown in plot B and plot D shows the spectra of equivalent circuit C with swept top and bottom resistance from 1 to 127 Ω.

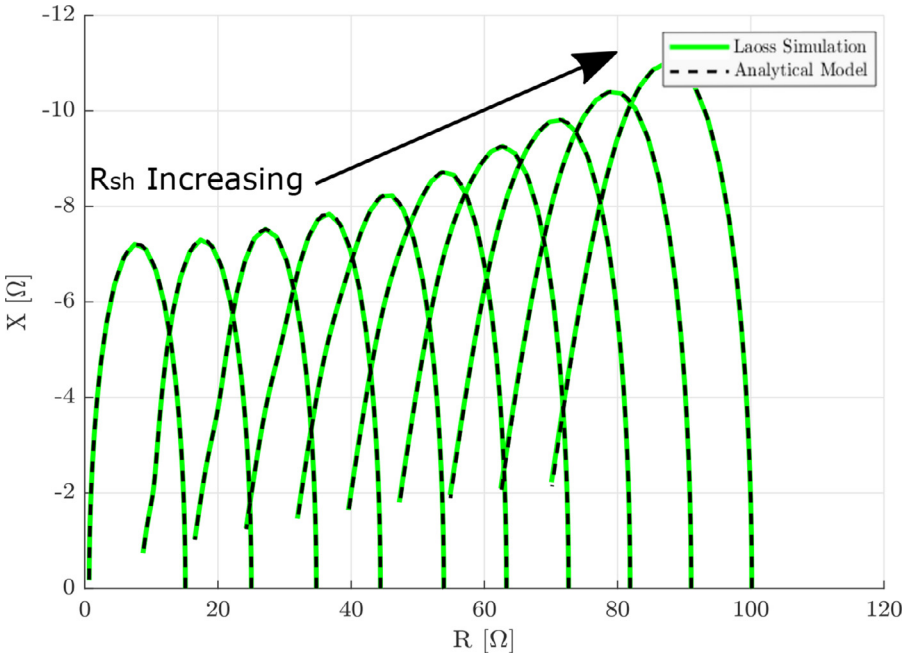

Fig. 4. Verification of the results of the time-harmonic FEM model and the 1D analytical model with identical domains, coupling laws and boundary conditions. The sheet resistance was varied from 1 to 136 Ω.

with $k^2 = 2Y(\omega)R_{sh}$. The detailed calculation steps leading to the expression in equation (18) are shown in the supplementary information.

Fig. 4 shows a Laoss AC simulation and the impedance of the analytical model with identical sheet resistance and coupling law in a Nyquist plot. The sheet resistance was swept from 1 to 136 Ω/sq.

It can be seen that the analytical model is an exact reproduction of the Laoss AC simulation for this particular geometry and verifies its correct implementation. One can see the increase of the linear ≈ 45° inclined high-frequency limit and the horizontal shift towards higher values on the x-axis, which is due to the contribution of the sheet resistance to the series resistance.

3.2. Model validation with differently sized silicon solar cells in steady-state

The main challenge in performing a simulation with our software tool is to find the optimal coupling law of the device. Ideally, the current-voltage characteristic and impedance of the smallest possible cell, which is not influenced by area effects such as potential drops, should be used.

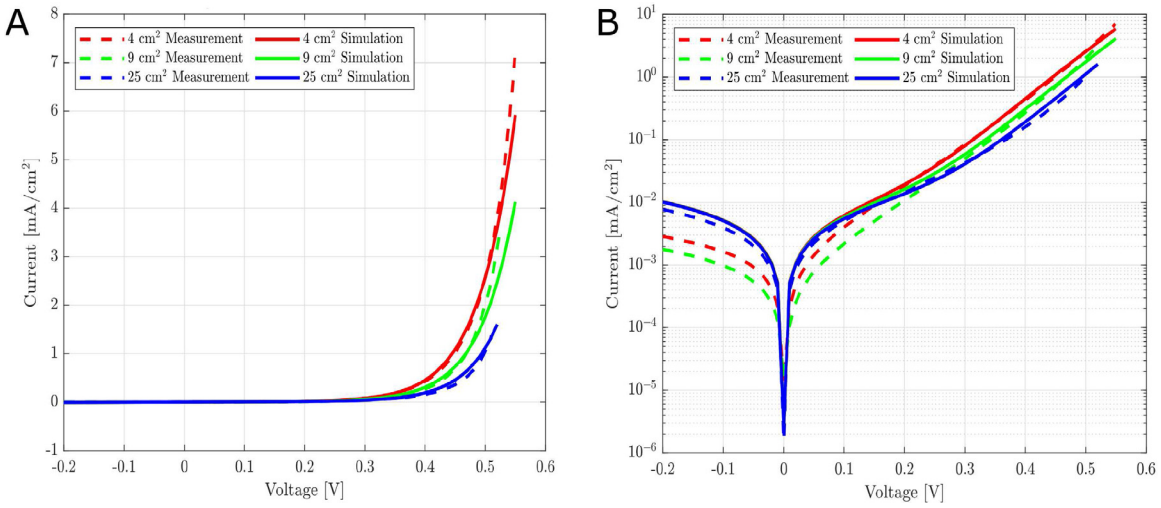

Fig. 5. Steady-state simulations (solid lines) and measurements (dashed lines) of 4 cm^2 (red), 9 cm^2 (green) and 25 cm^2 (blue) silicon solar cells (linear (A) and logarithmic (B) representation). (For interpretation of the references to colour in this figure legend, the reader is referred to the web version of this article.)

In order to mimic this, we have cut silicon cells with metal fingers into different sizes. Well conducting metal fingers, low contact resistance and busbars compensate for the sheet resistance of 94 Ω/sq on the top electrode, which leads to a low series resistance. This was confirmed by one-diode model fits in the dark (≈0.1 Ω), the intersection of the x-axis at high frequencies of impedance spectra and the mask dependent fill factor also indicated a low to non-existent series resistance [52] (see supplementary information).

When looking at the current density vs. voltage characteristics of the 4 cm^2, 9 cm^2 and 25 cm^2 cells in Fig. 5, a shift towards lower voltage with decreasing area can be observed. The effective series resistance is virtually zero due to the highly conductive metal grid enhanced top electrode as discussed above. Therefore, we would have expected the current density vs. voltage curves to be very similar for the different cell sizes. The shift towards lower voltage for a smaller active surface is reported to be related to increasing edge recombination effects per area. These are usually quantified with the two-diode model

$$J = J_{01}\left(e^{\frac{V-JR_s}{n_1 V_T}} - 1\right) + J_{02}\left(e^{\frac{V-JR_s}{n_2 V_T}} - 1\right) + \frac{V - JR_s}{R_p}, \tag{19}$$

where an increase of the second diode current J_{02} can be observed with increasing edge recombination [53,54]. Equation (19) describes the two-diode model in the dark, first introduced by Sah et al. [55]. The diffusion (J_{01}) and recombination currents are split into two diodes, taking recombination losses in the depletion region into account with the saturation current J_{02}. Further losses are considered with the series resistance R_s and the parallel resistance R_p, while $V_T = kT/q$ is the thermal voltage. The ideality factors are typically chosen as $n_1 = 1$ and $n_2 = 2$. We assume that the edge recombination effects have been amplified by laser cutting and grinding the cells.

In order to find a general coupling law of our solar cells, we had to modify the measured current-voltage law by correcting for edge effects. In a second step, we added them again on the boundaries of the domain during scaling simulations in Laoss, so that we could obtain an exact reproduction of the cell's conditions. This was done by fitting the two-diode model to the 25 cm^2 cell, which has the least edge effects per area, to gain the two-diode model parameters of the device. The edge effects were removed by lowering J_{02} (see supplementary information).

The geometry and fingers in Laoss were modelled according to the measured cells. An additional boundary surrounding the domain with an assumed width of 50 μm was added. At this point, it should be mentioned that the value of J_{02} varies when the chosen width of the surrounding boundary is changed.

The coupling law with the removed edge effects was used on the entire domain including the active area and under the fingers. On the boundary we additionally increased J_{02} to 0.2 A/m^2, while on the inner domain we kept J_{02} at a constant low value of 1e-6 A/m^2, by which a fit was achieved with the 25 cm^2 cell. As mentioned, the value of J_{02} depends on the width of the boundary surrounding the domain.

On the well conductive metal fingers and the aluminium backside (bottom electrode) a low sheet resistance of 1 mΩ/sq was chosen. Thereafter, only the area was adjusted to 4 cm^2 and 9 cm^2 to obtain the area dependent steady-state results shown in Fig. 5.

The agreement between measurement and simulation is evident and the trend of the curves shifting towards lower voltages with increasing edge recombination per area is clearly visible. At higher voltages the curves fit very well, while the semi-logarithmic plot at lower potentials shows that the parallel resistance of the cells is inconsistent. This deviation probably originates from laser cutting and manual grinding of the edges, which could lead to irregularities in parallel resistance. The simulated curves meet at about 0.1 V, since the parallel resistance of the fitted 25 cm^2 cell was used for all domain sizes.

In a next step, the 4 cm^2 cell was intentionally shunted with the laser by passing it several times over the same spot. To reproduce measurements of this shunted cell with simulations, a 0.02 mm^2 subdomain with shunt properties (ohmic 1D coupling law with specific conductivity) was added to the domain. Fig. 6A shows the map of the vertical current density obtained from the Laoss simulation (left, scaled to a maximum value of 300 A/m^2) that is linearly related [56] to the EL-image (electro luminescence) of the shunted 4 cm^2 silicon cell on the right hand side, taken at 0.7 V bias. The dark spot at the top of the EL-image had also been observed in the non-shunted cell (see supplementary information), which has not shown any signs of low parallel resistance. Consequently, we conclude that this is not a shunt, but another, seemingly non-conductive, defect. The busbar on the top side of the EL-image is not shown.

To simulate a purely ohmic shunt, an increased conductivity from the top to the bottom domain with a device thickness of 200 μm was chosen as a linear coupling law. As the coupling law of the 25 cm^2 cell was still used for this simulation, which has a lower parallel resistance than the 4 cm^2 device, the Laoss simulation inevitably leads to an overestimation of the shunt resistance. Without a parallel resistance correction of the coupling law, a fit with the shunted cell was achieved with a shunt resistance of 909 Ω (s. Fig. 6B), while with a for parallel resistance corrected coupling law the fitting shunt resistance dropped to 770 Ω.

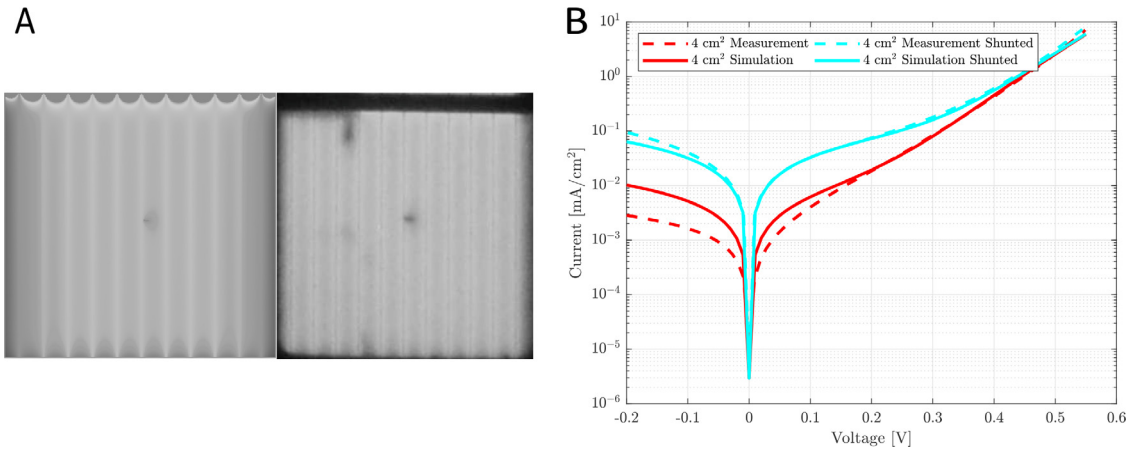

Fig. 6. Source current density of the top electrode from a steady-state simulation with shunt scaled to a maximum current of 300 A/m^2 (left) and an EL-image of the 4 cm^2 cell, both at 0.7 V bias (A). Steady-state simulations (solid lines) and measurements (dashed lines) of a 4 cm^2 cell before (red) and after being shunted (cyan) are shown in B. (For interpretation of the references to colour in this figure legend, the reader is referred to the web version of this article.)

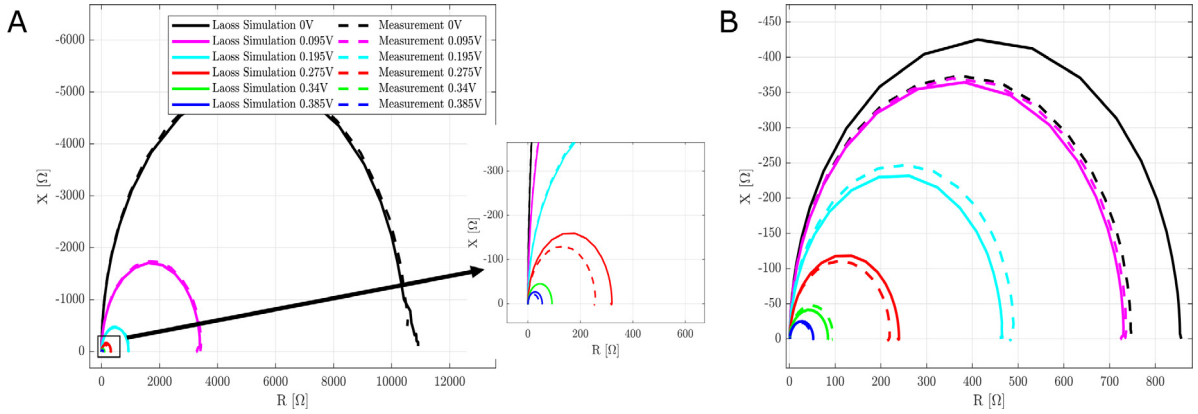

Fig. 7. Measured impedance spectra of the 4 cm^2 original silicon solar cell (A) and shunted (B) (dashed lines) and the simulation (solid lines) in a Nyquist representation.

3.3. Model validation with shunted silicon solar cells in AC

For the validation of the AC solver we took a closer look at the influence of shunts and bias voltages using the 4 cm^2 silicon cell. With the shunted and original 4 cm^2 cell we performed EIS measurements and reproduced them with the AC solver in Laoss. As explained in Section 2.2, the steady-state problem has to be solved first to provide the operating points needed for the linearisation of the AC problem. Therefore, the steady-state coupling laws remained identical to the ones used in Section 3.2. Additionally, frequency and bias voltage dependent impedance laws of the stack are added to perform a small-signal analysis in Laoss.

For the sake of simplification, the edge effects in the frequency domain have been neglected and measured impedance spectra of a 1 cm^2 cell, taken at 0, 0.101, 0.2, 0.29, 0.375 and 0.43 V, were used to perform the AC simulations. For the reproduction of the impedance spectra from the artificially shunted cell, the same shunt conductivity that has been used for the steady-state simulation, also defined the AC coupling law of the shunt in the AC simulations. Its conductivity was set to a constant value for the entire range of frequencies and voltages to represent an ohmic shunt resistance of 909 Ω.

For the simulated impedance spectra of the 4 cm^2 cell the frequency ranges from 1 Hz to 1 MHz and the bias potentials were set according to the bias potentials from the measurements to 0, 0.095, 0.195, 0.275, 0.34 and 0.385 V. The sheet resistance leads to a potential drop on the electrodes, which has to be considered when evaluating the coupling law. Laoss therefore uses spline interpolation to obtain the impedance values from the coupling law evaluated at the correct vertical potential drop.

The AC results of the original cell, shown in a Nyquist plot in Fig. 7A, agree very well with the measured spectra, only at 0.275 V bias the measurement deviates slightly from the simulation. Nevertheless, these simulated and measured spectra confirm the ability of our software to predict impedance measurement results of large-area devices with the data from small area cells.

It is clearly visible that the impedance spectra of the measured and simulated cell with a shunt in Fig. 7B shrank by a considerable amount, which is typical for shunted solar cells due to the decreasing parallel resistance [57]. Even though the spectra from the shunted cell show a deviation between measurement and simulation at 0 V bias, the simulation results are overall convincing. The intersection with the x-axis at low frequencies of the measured 0 V bias arc in Fig. 7B would be at ≈750 Ω, which is close to the fitted shunt resistance from the steady-state simulations of 770 Ω shown in Section 3.2.

4. Conclusion and outlook

To investigate the influence of defects, such as shunts, and resistive electrodes in the upscaling process of solar cells and OLEDs, we have extended the electrical steady-state model by a linearization for sinusoidal small-signal analysis in our software tool Laoss. With an analytical model of a simplistic domain we have verified the correct implementa-

tion of the AC module extension. Simulations show that the impedance arcs can no longer be interpreted in the same way as in small-area devices where the sheet resistance can be neglected. In large-area electrodes the sheet resistance influences size, position and shape of the resulting impedance arc. In contrast to the analytical AC model, the FEM simulation can be applied to study any device geometry and optional inhomogeneous layer properties. It thus is a versatile tool for solar cell characterization.

The constant and reliable fabrication of novel devices with various sizes is challenging, which complicates a validation with this type of cells. Therefore, we have laser-cut monocrystalline silicon solar cells into different sizes and shunted one device intentionally. Unfortunately, due to the optimized finger grid, these cells already had minimal influence of the sheet resistance and revealed peculiarities such as enhanced edge recombination effects. Using steady-state simulations, we have analyzed the size scaling of cells with an active area of 4, 9 and 25 cm^2. In addition, edge recombination and the presence of shunts were simulated and compared with experimental data with good agreement.

With simulations in the frequency domain, the influence of shunts at different bias voltages was predicted with a slightly larger discrepancy to the measured data between the shunted cell and the simulation at 0 V bias. Nevertheless, impedance spectroscopy offers the opportunity of a more detailed investigation of cell properties than current-voltage characteristics alone.

In upcoming studies, we plan to perform experiments in steady-state and frequency domain with novel devices, such as perovskite solar cells and investigate defects with dark lock-in thermography in addition to the presented EL imaging reported here. Impedance spectra of novel devices are usually more complicated to analyse as such of silicon solar cells due to multiple impedance arcs. Simulations are becoming increasingly helpful when multiple impedance arcs are involved in order to evaluate the individual processes of the devices.

A newly implemented thermal AC module will also allow for "lock-in thermography" simulations that demonstrate the influence of defects on temperature distributions. This is another way to quantify defects and demonstrate their influence on the electro-thermal properties of large-area devices.

Declaration of competing interest

The authors declare that they have no known competing financial interests or personal relationships that could have appeared to influence the work reported in this paper.

CRediT authorship contribution statement

Ennio Luigi Comi: Conceptualization, Data curation, Investigation, Writing – original draft, Visualization, Validation, Methodology. **Evelyne Knapp:** Conceptualization, Methodology, Supervision, Writing – review & editing. **Stefano Weidmann:** Software, Validation. **Christoph Kirsch:** Software, Supervision, Writing – review & editing. **Sandra Jenatsch:** Conceptualization, Investigation, Writing – review & editing. **Roman Hiestand:** Software. **Beat Ruhstaller:** Conceptualization, Supervision, Writing – review & editing.

Acknowledgement

The authors would like to thank Hartmut Nussbaumer, Jan Meister and Franz Baumgartner from the Institute of Energy Systems and Fluid Engineering (IEFE) at ZHAW School of Engineering for providing the silicon solar cell samples and carrying out EL imaging measurements as well as Ralf Hiptmair from the Federal Institute of Technology Zurich (ETHZ) for fruitful discussions. Financial support for H2020 project CORNET (contract no. 760949) and for the Innosuisse project AIPV (project no. 37304.1 IP) is gratefully acknowledged.

Appendix A. Supplementary Information

A1. Mask dependent fill factor

In Section 3.2, we claimed that the differences between the current-voltage characteristics of differently sized devices do not originate from an increase in series resistance, as the mask dependent fill factor indicates a low series resistance. Here we aim to explain how the solar cell's series resistance influences the results of masking the solar cells.

Kiermasch et al. [52] recently published a research paper about the effects of masking on V_{oc} and FF in solar cells, where the following formula was postulated:

$$\Delta V_{oc} = \frac{nkT}{q} \cdot \ln(\alpha) \quad \text{with} \quad \alpha = \frac{A_{aperture}}{A_{cell}}. \tag{A.1}$$

According to Kiermasch et al. the difference in V_{oc} originates from the inequality between generation and recombination current density at open-circuit voltage. This inequality occurs because the non-illuminated part of the masked cell will join in as semiconductor volume for carrier recombination. With this reasoning the masking of a solar cell causes an open-circuit voltage drop, which is comparable with an unmasked cell with reduced illumination intensity. The postulated formula for V_{oc} deviation is based on the general analytic expression for the V_{oc} of a solar cell with the addition of a masking aperture ratio α multiplied with the light generated current.

Kiermasch et al. also modified Green's empirical expression for the fill factor published in 1981 [58] to evaluate the fill factor's dependency on masking. Equation (A.2) describes the FF of an ideal cell without series resistance and the FF of a non-ideal cell suffering from series resistance is shown in equation (A.3)

$$FF_{ideal,masked} = \frac{\ln\left(\frac{\alpha \cdot J_{sc}}{I_0}\right) - \ln\left(ln\left(\frac{\alpha \cdot J_{sc}}{I_0}\right) + 0.72\right)}{ln\left(\frac{\alpha \cdot J_{sc}}{I_0}\right) + 1} \tag{A.2}$$

$$FF_{series,masked} = FF_{ideal,masked}\left(1 - \frac{R_s \cdot J_{sc} \cdot \alpha}{ln\left(\frac{\alpha \cdot J_{sc}}{I_0}\right) \cdot \frac{nkT}{q}}\right). \tag{A.3}$$

Fig. A.1 shows the theoretical ideal mask dependent fill factor. It is visible that for an ideal cell the FF will decrease the more the illu-

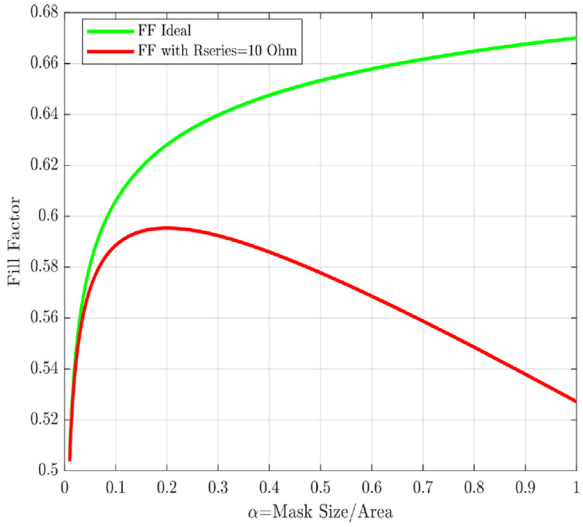

Fig. A.1. Ideal mask dependent FF (green) and non-ideal mask dependent FF with 10 Ω series resistance (red) plotted with a set of one-diode model parameters from a dark current voltage characteristic (n=3, Isc=14.5 mA/cm^2, I0=0.002 mA/cm^2). (For interpretation of the references to colour in this figure legend, the reader is referred to the web version of this article.)

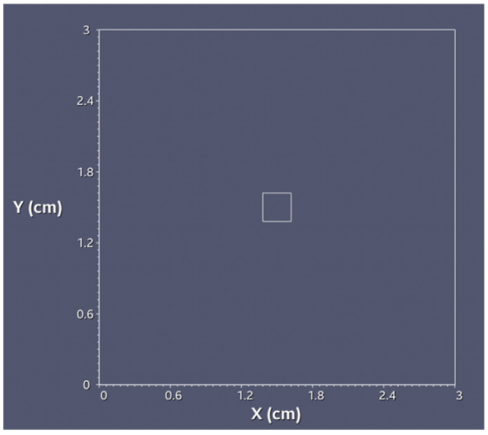

Fig. A.2. Geometry used to simulate the mask dependent FF and V_{oc} with the illuminated coupling law in the center and the dark current-voltage curve on the outside.

minated area shrinks. In a non-ideal cell, the FF will increase up to a certain level due to reduced ohmic losses at lower current densities. As shown in Fig. A.2, we reconstructed the masking of a solar cell in our software by adding a mask to the geometry. The rectangle in the center is the illuminated part, containing the full area measurement of the 9 cm^2 cell taken at 0.1 sun as local current-voltage law. The surrounding domain, which is representing the mask, contains the dark current-voltage characteristic of the 9 cm^2 cell as local current-voltage law. The sheet resistance was neglected. By varying the size of the illuminated subdomain, the mask dependency of the V_{oc} and FF could be simulated with our software tool as shown in Fig. A.3. As the FF is not increasing with a decreasing masking aperture ratio, we conclude that the series resistance of these silicon solar cells is indeed low.

A2. Analytical 1D model with bias voltage independent AC coupling law

The FEM results shown in Fig. 2 have been reproduced with an analytical model of a simple symmetric 1D domain as an alternative modelling approach. In a previous publication by Lanz et al. [51] we developed a similar analytical model for an illuminated solar cell in steady-state. Here, we outline the detailed calculation steps behind the analytical impedance expression.

We assume identical quadratic domains on the top and bottom electrode with side length L and an identical sheet resistance R_{sh} on both electrodes. The boundary conditions are chosen such that the problem can be treated in one dimension and all derivatives in y-direction vanish.

The ODEs describing the voltage distribution in the top and bottom electrode in the dark are defined as follows:

$$R_{sh}^{T\,-1}\frac{d^2}{dx^2}\varphi^T = Y(\omega)(\varphi^T - \varphi^B) \tag{A.4}$$

$$R_{sh}^{B\,-1}\frac{d^2}{dx^2}\varphi^B = -Y(\omega)(\varphi^T - \varphi^B) \tag{A.5}$$

Dirichlet boundary conditions for constant voltage at $x = L$ and $x = 0$ on opposing electrodes, standing for the applied bias potential V_{bias}, and Neumann conditions with $E = 0$ and therefore zero current flux on the remaining boundaries are added. In this particular case, the frequency-dependent admittance $Y(\omega)$ is coupling the two domains with a bias voltage-independent conductance and susceptance. By recasting the system of ODEs and using $\varphi^T \pm \varphi^B$ as unknown quantity we can rewrite equations (A.4) and (A.5) as

$$\frac{d^2}{dx^2}(\varphi^T + \varphi^B) = 0 \tag{A.6}$$

$$\frac{d^2}{dx^2}(\varphi^T - \varphi^B) = k^2(\varphi^T - \varphi^B) \tag{A.7}$$

with $k^2 = 2Y(\omega)R_{sh}$. The unique solutions of the ODEs for the top and bottom electrode look as follows:

$$\varphi^T + \varphi^B = V_{bias}\frac{2\left(kx\sinh\left(\frac{kL}{2}\right) + \cosh\left(\frac{kL}{2}\right)\right)}{kL\sinh\left(\frac{kL}{2}\right) + 2\cosh\left(\frac{kL}{2}\right)} \tag{A.8}$$

$$\varphi^T - \varphi^B = V_{bias}\frac{2\cosh\left(\frac{1}{2}k(L-2x)\right)}{kL\sinh\left(\frac{kL}{2}\right) + 2\cosh\left(\frac{kL}{2}\right)} \tag{A.9}$$

The impedance is then computed by integrating the potential difference along the x-axis. This results in the following analytical impedance expression for this simplistic domain

$$Z = \frac{V_{bias}}{LY(\omega)\int_0^L(\varphi^T - \varphi^B)dx} = \frac{R_{sh}\left(2\coth\left(\frac{kL}{2}\right) + kL\right)}{2kL}. \tag{A.10}$$

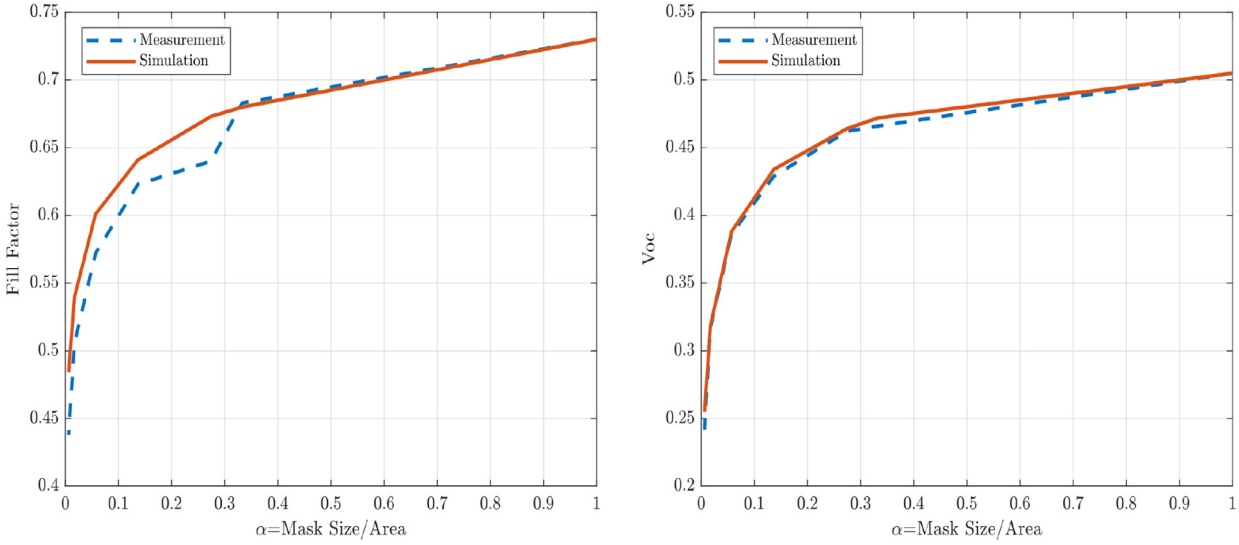

Fig. A.3. Mask dependent FF and V_{oc}, measured and simulated in Laoss.

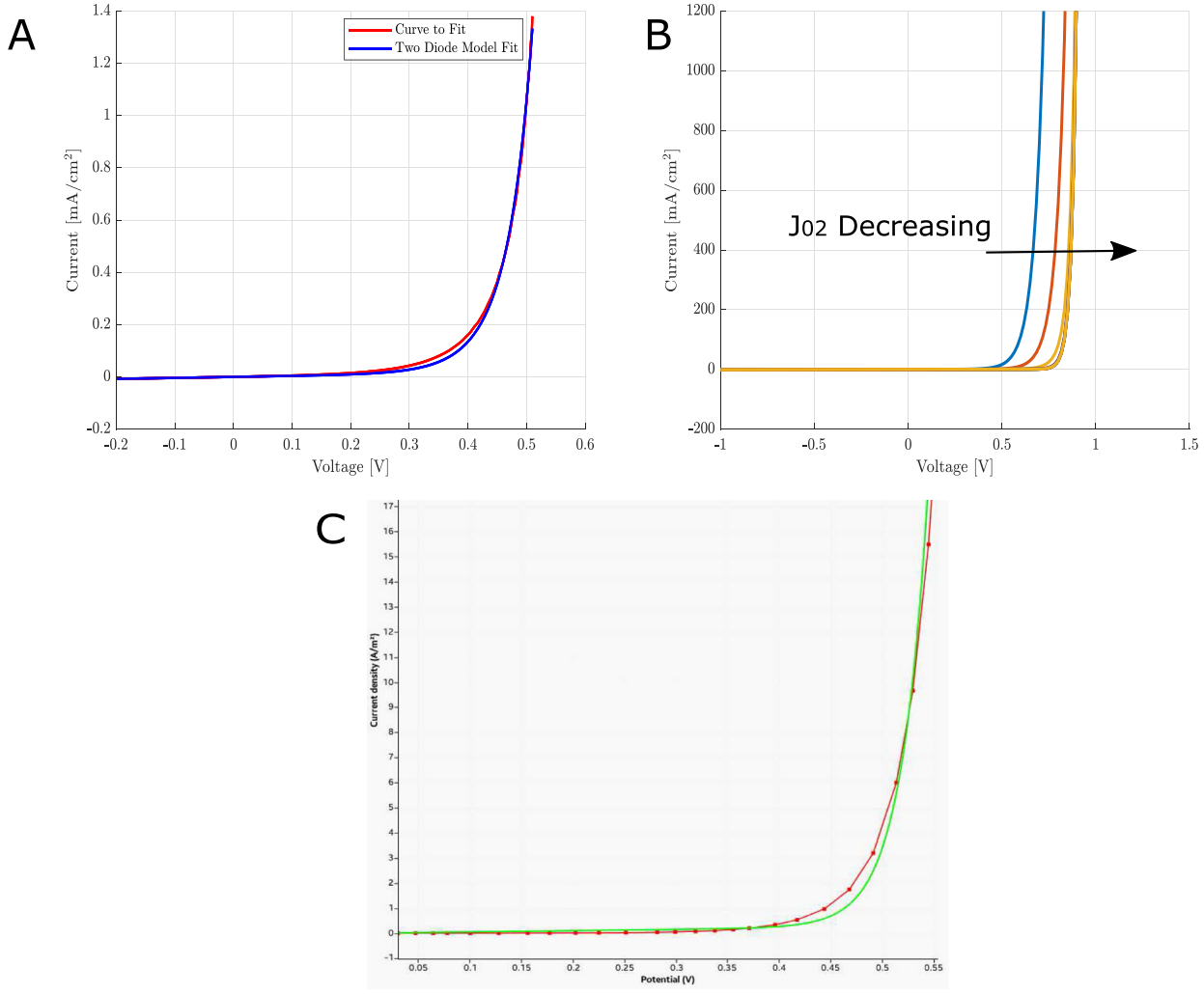

Fig. A.4. Fitting result with the two-diode model of the 25 cm^2 silicon solar cell (A). With increasing J_{02}, the curve shifts towards higher voltages until a saturation is reached (B). The corrected current-voltage characteristic (green) and the current-voltage characteristic from the datasheet (red) is shown in C. (For interpretation of the references to colour in this figure legend, the reader is referred to the web version of this article.)

The bias voltage independent AC coupling law is based on the following conductance G and susceptance B of the admittance:

$$Y(\omega) = G + iB(\omega) = 480.941\,\frac{S}{m^2} + i\omega \cdot 0.00808\,\frac{F}{m^2} \tag{A.11}$$

Since this AC coupling law does not depend on a bias voltage and the same coupling law is applied for all bias voltages, the current-voltage characteristic of the coupling law becomes redundant for the AC simulation result and can therefore be freely chosen. Consequently, the steady-state equations (12) and (13) do not have to be solved in this case and the AC equations (14) and (15) become independent of $\varphi^{T,B}_{bias}$.

The parameters required by Laoss for the AC coupling law are therefore only the frequency, conductance and susceptance.

A3. Correction for edge recombination in current-voltage characteristic

To find a general coupling law of the laser cut silicon cells, we had to modify the measured current-voltage law by correcting for edge recombination effects. We added the edge recombination again on a geometry surrounding the boundary with 50 µm width in Laoss with an increased J_{02} (see Section 3.2).

The curve was fitted with the trust-region-reflective optimization algorithm, which is implemented in Matlab. The resulting characteristic is shown in Fig. A.4A and the resulting parameters are listed in Table A.1.

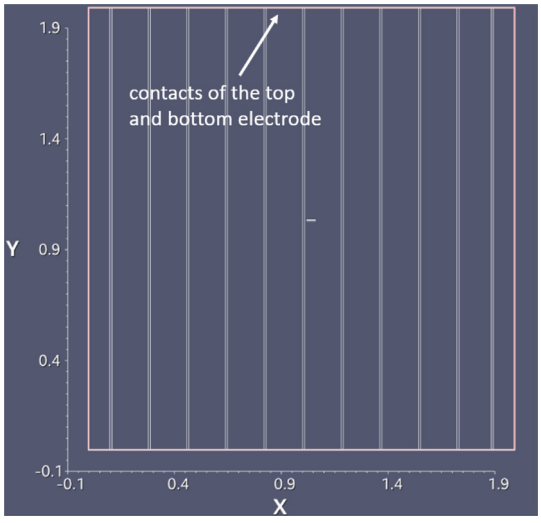

Fig. A.5. Shunted 4 cm^2 geometry used in Laoss for simulations with the surrounding edge colored in red. The domains without shunt with 9 cm^2 and 25 cm^2 active area are shown in B and C. (For interpretation of the references to colour in this figure legend, the reader is referred to the web version of this article.)

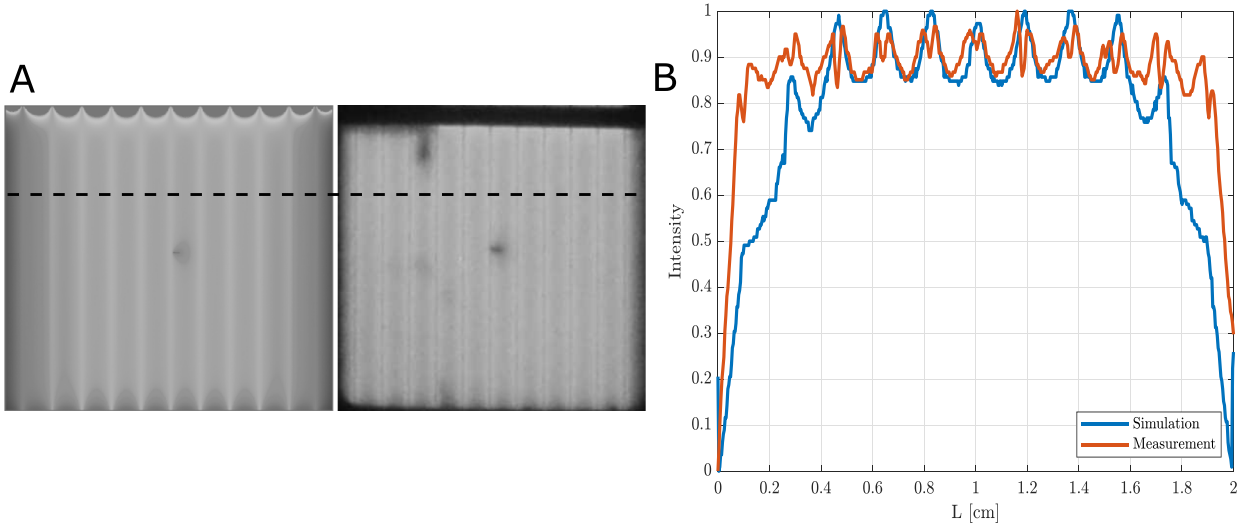

Fig. A.6. Source current density of the top electrode from a Laoss steady-state simulation with shunt scaled to a maximum current of 300 A/m^2 (left) and an EL-image of the 4 cm^2 cell both at 0.7 V bias (A). The cross section of the light and current intensity of the shunted 4 cm^2 solar cell scaled to 1 is shown in B.

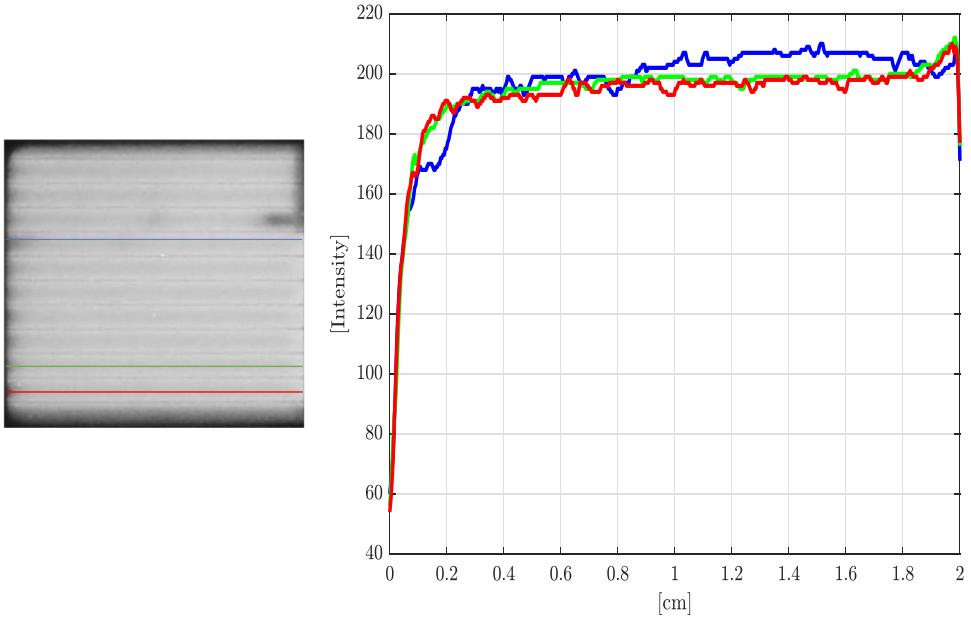

Fig. A.7. Measured vertical intensity EL profiles of the original 4 cm^2 cell. The increase in intensity is not uniformly distributed around the domain.

Table A.1
Fitting result with the two-diode model of the 25 cm^2 silicon solar cell.

Parameter	Value	Unit
J_{01}	1.27e-8	A/m^2
J_{02}	4.99e-4 → 1e-6	A/m^2
n_1	1	
n_2	2	
J_{sc}	2.94e-4	A/m^2
R_s	0.1	Ω
R_p	1050	Ω
T	300	K

The saturation current of the second diode J_{02} was lowered from 4.99e-4 to 1e-6 A/m^2. Depending on the remaining two-diode model parameters, a saturation is achieved when J_{02} decreases. This is shown in Fig. A.4B. The series resistance was neglected in the coupling law, as we assume that the total series resistance originates from the sheet resistance which Laoss accounts for and is an input parameter for the simulation.

To check whether the corrected current-voltage characteristic is realistic, we have compared it to the current-voltage characteristic from the solar cell suppliers data sheet. We subtracted the photocurrent J_{sc} to obtain the dark curve. This comparison is shown in Fig. A.4C.

In summary, we corrected the current-voltage measurement for edge recombination for the coupling law in the active area and added the edge recombination again to the geometry surrounding boundary.

A4. Utilized geometries in laoss

The 4 cm^2 geometry used for scaling and AC simulations is shown in Fig. A.5. According to the original device, the contacts of the top and bottom electrode with applied Dirichlet boundary conditions are placed on the upper end of the domain.

A5. EL-images and simulated source current density

As mentioned in Section 3.2, an EL-image and the current density of a solar cell (s. Fig. A.6A) are linearly related [56]. Fig. A.6B shows a cross section of the normalized EL and current intensity of the shunted 4 cm^2 solar cell.

The intensity dips between the gridlines in the cell's center are well reproduced by Laoss except under the fingers, where Laoss shows the highest current density, while the fingers show a dark stripe in the EL-image. This is to be expected since the simulated current is maximum below the metal grid and the experimental image, however, suffers from shading due to the metal grid lines. The current-to-luminance conversion efficiency would have to be set to zero at the grid line domains to account for shading in the model. The intensity on the left and right boundaries drops significantly more in the Laoss simulation compared to the EL-image. This drop is mainly caused by the added edge recombination effects to the geometry in Laoss. In the simulation we assume that the edge recombination in the silicon solar cells is evenly distributed around the cell. In the measurement however, vertical intensity profiles indicate that not all edges are affected by edge recombination to the same extent (s. Fig. A.7) and therefore this intensity dip on the left and right boundary is not as pronounced as in the current density simulation.

In Fig. A.6A the EL measurement shows a second dark spot above the dotted line which is not present in the simulation. The spot is also visible in the EL-image of the not shunted original 4 cm^2 cell as shown in Fig. A.7. The dark spot on top of the domain is probably not a shunt as the current-voltage characteristic and impedance spectra of the 4 cm^2 cell does not show any signs of a low parallel resistance. The dark spot probably originates from a high recombination region, which is caused by bulk or surface defects [59] or from a non-conducting defect.

References

[1] C. Kost, T. Schlegl, J. Thomsen, S. Nold, J. Mayer, N. Hartmann, C. Senkpiel, S. Philipps, S. Lude, N. Saad, Fraunhofer ISE: levelized cost of electricity - renewable energy technologies, march 2018, Fraunhofer ISE Levelized Cost Electr. - Renew. Energy Technol. (March) (2018).

[2] M.A. Green, Y. Hishikawa, W. Warta, E.D. Dunlop, D.H. Levi, J. Hohl-Ebinger, A.W. Ho-Baillie, Solar cell efficiency tables (version 50), Prog. Photovoltaics Res. Appl. 25 (7) (2017) 668–676, doi:10.1002/pip.2909.

[3] NREL, Best Research-Cell Efficiencies: Rev. 08-18-2021, 2020.

[4] D. Yang, R. Yang, X. Ren, X. Zhu, Z. Yang, C. Li, S.F. Liu, Hysteresis-Suppressed high-Efficiency flexible perovskite solar cells using solid-State ionic-Liquids for effective electron transport, Adv. Mater. 28 (26) (2016) 5206–5213, doi:10.1002/adma.201600446.

[5] G. Nogay, F. Sahli, J. Werner, R. Monnard, M. Boccard, M. Despeisse, F.-J. Haug, Q. Jeangros, A. Ingenito, C. Ballif, 25.1%-Efficient Monolithic perovskite/silicon tandem solar cell based on a p -type monocrystalline textured silicon wafer and high-Temperature passivating contacts, ACS Energy Lett. 4 (4) (2019) 844–845, doi:10.1021/acsenergylett.9b00377.

[6] J. Werner, C.H. Weng, A. Walter, L. Fesquet, J.P. Seif, S. De Wolf, B. Niesen, C. Ballif, Efficient monolithic perovskite/silicon tandem solar cell with cell area >1 cm^2, J. Phys. Chem. Lett. 7 (1) (2016) 161–166, doi:10.1021/acs.jpclett.5b02686.

[7] D. Bi, W. Tress, M.I. Dar, P. Gao, J. Luo, C. Renevier, K. Schenk, A. Abate, F. Giordano, J.-P. Correa Baena, J.-D. Decoppet, S.M. Zakeeruddin, M.K. Nazeeruddin, M. Grätzel, A. Hagfeldt, Efficient luminescent solar cells based on tailored mixed-cation perovskites, Sci. Adv. 2 (1) (2016) e1501170, doi:10.1126/sciadv.1501170.

[8] OXFORDPV, Oxford PV perovskite solar cell achieves 28% efficiency, Oxfort PV (December 2018) (2018) 20–23.

[9] J. Zheng, H. Mehrvarz, F.-J. Ma, C.F.J. Lau, M.A. Green, S. Huang, A.W.Y. Ho-Baillie, 21.8% Efficient monolithic perovskite/homo-Junction-Silicon tandem solar cell on 16 cm 2, ACS Energy Lett. 3 (9) (2018) 2299–2300, doi:10.1021/acsenergylett.8b01382.

[10] J. Zheng, C.F.J. Lau, H. Mehrvarz, F.-J. Ma, Y. Jiang, X. Deng, A. Soeriyadi, J. Kim, M. Zhang, L. Hu, X. Cui, D.S. Lee, J. Bing, Y. Cho, C. Chen, M.A. Green, S. Huang, A.W.Y. Ho-Baillie, Large area efficient interface layer free monolithic perovskite/homo-junction-silicon tandem solar cell with over 20% efficiency, Energy Environ. Sci. 11 (9) (2018) 2432–2443, doi:10.1039/C8EE00689J.

[11] J. Zheng, H. Mehrvarz, C. Liao, J. Bing, X. Cui, Y. Li, V.R. Gonçales, C.F.J. Lau, D.S. Lee, Y. Li, M. Zhang, J. Kim, Y. Cho, L.G. Caro, S. Tang, C. Chen, S. Huang, A.W.Y. Ho-Baillie, Large-Area 23%-Efficient monolithic perovskite/homojunction-Silicon tandem solar cell with enhanced UV stability using down-Shifting material, ACS Energy Lett. 4 (11) (2019) 2623–2631, doi:10.1021/acsenergylett.9b01783.

[12] S. He, L. Qiu, L.K. Ono, Y. Qi, How far are we from attaining 10-year lifetime for metal halide perovskite solar cells? Mater. Sci. Eng. R Reports 140 (January) (2020) 100545, doi:10.1016/j.mser.2020.100545.

[13] Z. Li, T.R. Klein, D.H. Kim, M. Yang, J.J. Berry, M.F.A.M. van Hest, K. Zhu, Scalable fabrication of perovskite solar cells, Nat. Rev. Mater. 3 (4) (2018) 18017, doi:10.1038/natrevmats.2018.17.

[14] M.R. Leyden, Y. Jiang, Y. Qi, Chemical vapor deposition grown formamidinium perovskite solar modules with high steady state power and thermal stability, J. Mater. Chem. A 4 (34) (2016) 13125–13132, doi:10.1039/C6TA04267H.

[15] Y. Galagan, E.W.C. Coenen, W.J.H. Verhees, R. Andriessen, Towards the scaling up of perovskite solar cells and modules, J. Mater. Chem. A 4 (15) (2016) 5700–5705, doi:10.1039/C6TA01134A.

[16] M. Kim, J. Kim, Y.-J. Lee, M. Ju, C. Park, N. Balaji, S. Lee, J. Kim, J. Yi, High sheet resistance emitter c-Si solar cells with low SRV by local line contact with transparent conducting oxides, Mater. Lett. 116 (2014) 258–261, doi:10.1016/j.matlet.2013.11.025.

[17] M.J. Kerr, J. Schmidt, A. Cuevas, J.H. Bultman, Surface recombination velocity of phosphorus-diffused silicon solar cell emitters passivated with plasma enhanced chemical vapor deposited silicon nitride and thermal silicon oxide, J. Appl. Phys. 89 (7) (2001) 3821–3826, doi:10.1063/1.1350633.

[18] N. Chen, K. Tate, A. Ebong, Generalized analysis of the impact of emitter sheet resistance on silicon solar cell performance, Jpn. J. Appl. Phys. 54 (8S1) (2015) 08KD20, doi:10.7567/JJAP.54.08KD20.

[19] S. Liu, X. Niu, W. Shan, W. Lu, J. Zheng, Y. Li, H. Duan, W. Quan, W. Han, C. Wronski, D. Yang, Improvement of conversion efficiency of multicrystalline silicon solar cells by incorporating reactive ion etching texturing, Sol. Energy Mater. Sol. Cells 127 (2014) 21–26, doi:10.1016/j.solmat.2014.04.001.

[20] B. Wilkinson, N.L. Chang, M.A. Green, A.W. Ho-Baillie, Scaling limits to large area perovskite solar cell efficiency, Prog. Photovoltaics Res. Appl. 26 (8) (2018) 659–674, doi:10.1002/pip.3035.

[21] B.A. Kamino, B. Paviet-Salomon, S.-j. Moon, N. Badel, J. Levrat, G. Christmann, A. Walter, A. Faes, L. Ding, J.J. Diaz Leon, A. Paracchino, M. Despeisse, C. Ballif, S. Nicolay, Low-Temperature screen-Printed metallization for the scale-Up of two-Terminal perovskitesilicon tandems, ACS Appl. Energy Mater. 2 (5) (2019) 3815–3821, doi:10.1021/acsaem.9b00502.

[22] AG Fluxim, Large Area Organic Semiconductor Simulation, (LAOSS) (2020).

[23] C. Kirsch, S. Altazin, R. Hiestand, T. Beierlein, R. Ferrini, T. Offermans, L. Penninck, B. Ruhstaller, Electrothermal simulation of large-Area semiconductor devices, Int. J. Multiphys. 11 (2) (2017) 127–136, doi:10.21152/1750-9548.11.2.127.

[24] D. Braga, S. Jenatsch, L. Penninck, R. Hiestand, M. Diethelm, S. Altazin, C. Kirsch, B. Ruhstaller, 3.3: Modeling electrical and optical crosstalk between adjacent pixels in organic lightemitting diode displays, SID Symp. Dig. Tech. Pap. 50 (S1) (2019) 31–34, doi:10.1002/sdtp.13374.

[25] M. Diethelm, L. Penninck, S. Altazin, R. Hiestand, C. Kirsch, B. Ruhstaller, Quantitative analysis of pixel crosstalk in AMOLED displays, J. Inf. Disp. 19 (2) (2018) 61–69, doi:10.1080/15980316.2018.1428232.

[26] M. Diethelm, L. Penninck, M. Regnat, T. Offermans, B. Zimmermann, C. Kirsch, R. Hiestand, S. Altazin, B. Ruhstaller, Finite element modeling for analysis of electroluminescence and infrared images of thin-film solar cells, Sol. Energy 209 (May) (2020) 186–193, doi:10.1016/j.solener.2020.08.058.

[27] A. Shah, Photovoltaic technology: the case for thin-Film solar cells, Science (80-.). 285 (5428) (1999) 692–698, doi:10.1126/science.285.5428.692.

[28] S.W. Glunz, F. Feldmann, A. Richter, M. Bivour, C. Reichel, H. Steinkemper, J. Benick, M. Hermle, The irresistible charm of a simple current flow pattern 25% with a solar cell featuring a full-Area back contact, Proc. 31st Eur. Photovolt. Sol. Energy Conf. Exibition (September) (2015) 259–263, doi:10.4229/EU-PVSEC20152015-2BP.1.1.

[29] S. Meier, P. Saint-Cast, N. Wöhrle, A. Fell, J. Greulich, A. Wolf, S.W. Glunz, Internal resistance of rear totally diffused solar cells with line shaped contacts, J. Appl. Phys. 122 (18) (2017) 183102, doi:10.1063/1.4999685.

[30] A. Fell, P.P. Altermatt, Detailed 3D full-cell modeling in Quokka3: Quantifying edge and solder-pad losses in an industrial PERC cell, in: AIP Conf. Proc., 1999, 2018, p. 020007, doi:10.1063/1.5049246.

[31] J. Zhao, A. Wang, M. Green, Series resistance caused by the localized rear contact in high efficiency silicon solar cells, Sol. Energy Mater. Sol. Cells 32 (1) (1994) 89–94, doi:10.1016/0927-0248(94)90258-5.

[32] F. Granek, M. Hermle, Enhanced lateral current transport via the front n + diffused layer of n-type high-efficiency back-junction back-contact silicon solar cells, Prog. Photovoltaics Res. Appl. 17 (1) (2009) 47–56, doi:10.1002/pip.862.

[33] P. Magnone, M. Debucquoy, D. Giaffreda, N. Posthuma, C. Fiegna, Understanding the influence of busbars in large-Area IBC solar cells by distributed SPICE simulations, IEEE J. Photovoltaics 5 (2) (2015) 552–558, doi:10.1109/JPHOTOV.2015.2392939.

[34] M. Dahlinger, K. Carstens, Optimized laser doped back surface field for IBC solar cells, Energy Procedia 92 (2016) 450–456, doi:10.1016/j.egypro.2016.07.126.

[35] A. Fell, K.C. Fong, K.R. McIntosh, E. Franklin, A.W. Blakers, 3-D Simulation of interdigitated-Back-Contact silicon solar cells with quokka including perimeter losses, IEEE J. Photovoltaics 4 (4) (2014) 1040–1045, doi:10.1109/JPHOTOV.2014.2320302.

[36] H. Nesswetter, P. Lugli, A.W. Bett, C.G. Zimmermann, Electroluminescence and photoluminescence characterization of multijunction solar cells, in: 2012 IEEE 38th Photovolt. Spec. Conf. PART 2, IEEE, 2012, pp. 1–6, doi:10.1109/PVSC-Vol2.2012.6656769.

[37] J. Renshaw, M.H. Kang, V. Meemongkolkiat, A. Rohatgi, D. Carlson, M. Bennett, 3D-Modeling of a back point contact solar cell structure with a selective emitter, Conf. Rec. IEEE Photovolt. Spec. Conf. (2009) 000375–000379, doi:10.1109/PVSC.2009.5411661.

[38] D.A. Jacobs, H. Shen, F. Pfeffer, J. Peng, T.P. White, F.J. Beck, K.R. Catchpole, The two faces of capacitance: new interpretations for electrical impedance measurements

of perovskite solar cells and their relation to hysteresis, J. Appl. Phys. 124 (22) (2018) 225702, doi:10.1063/1.5063259.
[39] I. Zarazua, G. Han, P.P. Boix, S. Mhaisalkar, F. Fabregat-Santiago, I. Mora-Seró, J. Bisquert, G. Garcia-Belmonte, Surface recombination and collection efficiency in perovskite solar cells from impedance analysis, J. Phys. Chem. Lett. 7 (24) (2016) 5105–5113, doi:10.1021/acs.jpclett.6b02193.
[40] M.T. Neukom, A. Schiller, S. Züfle, E. Knapp, J. Ávila, D. Pérez-del Rey, C. Dreessen, K.P. Zanoni, M. Sessolo, H.J. Bolink, B. Ruhstaller, Consistent device simulation model describing perovskite solar cells in steady-State, transient, and frequency domain, ACS Appl. Mater. Interfaces 11 (26) (2019) 23320–23328, doi:10.1021/acsami.9b04991.
[41] X. Xu, Z. Liu, Z. Zuo, M. Zhang, Z. Zhao, Y. Shen, H. Zhou, Q. Chen, Y. Yang, M. Wang, Hole selective NiO contact for efficient perovskite solar cells with carbon electrode, Nano Lett. 15 (4) (2015) 2402–2408, doi:10.1021/nl504701y.
[42] A. Ben Jazia Kharrat, M. Bourouina, N. Moutia, K. Khirouni, W. Boujelben, Gd doping effect on impedance spectroscopy properties of sol-gel prepared pr0.5-xgdxsr0.5Mno3 perovskites, J. Alloys Compd. 741 (2018) 723–733, doi:10.1016/j.jallcom.2018.01.236.
[43] E. Knapp, B. Ruhstaller, Analysis of negative capacitance and self-heating in organic semiconductor devices, J. Appl. Phys. 117 (13) (2015) 135501, doi:10.1063/1.4916981.
[44] J. Haschke, G. Christmann, C. Messmer, M. Bivour, M. Boccard, C. Ballif, Lateral transport in silicon solar cells, J. Appl. Phys. 127 (11) (2020) 114501, doi:10.1063/1.5139416.
[45] S. Laux, Techniques for small-signal analysis of semiconductor devices, IEEE Trans. Electron Devices 32 (10) (1985) 2028–2037, doi:10.1109/T-ED.1985.22235.
[46] S. Weidmann, Frequency Domain 2D + 1D FEM Simulation of Solar Cells - Master Thesis (2019).
[47] AG Fluxim, Platform for all-in-one characterization, (PAIOS) (2020).
[48] S. Züfle, R. Hansson, E.A. Katz, E. Moons, Initial photo-degradation of PCDTBT:PC70bm solar cells studied under various illumination conditions: role of the hole transport layer, Sol. Energy 183 (March) (2019) 234–239, doi:10.1016/j.solener.2019.03.020.
[49] F. Fabregat-Santiago, J. Bisquert, G. Garcia-Belmonte, G. Boschloo, A. Hagfeldt, Influence of electrolyte in transport and recombination in dye-sensitized solar cells studied by impedance spectroscopy, Sol. Energy Mater. Sol. Cells 87 (1–4) (2005) 117–131, doi:10.1016/j.solmat.2004.07.017.
[50] A.B.F. Martinson, M.S. Goes, F. Fabregat-Santiago, J. Bisquert, M.J. Pellin, J.T. Hupp, Electron transport in dye-Sensitized solar cells based on ZnO nanotubes: evidence for highly efficient charge collection and exceptionally rapid dynamics, J. Phys. Chem. A 113 (16) (2009) 4015–4021, doi:10.1021/jp810406q.
[51] T. Lanz, M. Bonmarin, M. Stuckelberger, C. Schlumpf, C. Ballif, B. Ruhstaller, Electrothermal finite-Element modeling for defect characterization in thin-Film silicon solar modules, IEEE J. Sel. Top. Quantum Electron. 19 (5) (2013) 1–8, doi:10.1109/JSTQE.2013.2250259.
[52] D. Kiermasch, L. Gil-Escrig, H.J. Bolink, K. Tvingstedt, Effects of masking on open-Circuit voltage and fill factor in solar cells, Joule 3 (1) (2019) 16–26, doi:10.1016/j.joule.2018.10.016.
[53] D. Bertrand, S. Manuel, M. Pirot, A. Kaminski-Cachopo, Y. Veschetti, Modeling of edge losses in al-BSF silicon solar cells, IEEE J. Photovoltaics 7 (1) (2017) 78–84, doi:10.1109/JPHOTOV.2016.2618603.
[54] K.R. McIntosh, Lumps, Humps and Bumps: Three Detrimental Effects in the Current-Voltage Curve of Silicon Solar Cells, 2001 Ph.D. thesis.
[55] C.T. Sah, R.N. Noyce, W. Shockley, Carrier generation and recombination in P-N junctions and P-N junction characteristics, Proc. IRE 45 (9) (1957) 1228–1243, doi:10.1109/JRPROC.1957.278528.
[56] J. Kalinowski, N. Camaioni, P. Di Marco, V. Fattori, A. Martelli, Kinetics of charge carrier recombination in organic light-emitting diodes, Appl. Phys. Lett. 72 (5) (1998) 513–515, doi:10.1063/1.120805.
[57] N. Katayama, S. Osawa, S. Matsumoto, T. Nakano, M. Sugiyama, Degradation and fault diagnosis of photovoltaic cells using impedance spectroscopy, Sol. Energy Mater. Sol. Cells 194 (September 2018) (2019) 130–136, doi:10.1016/j.solmat.2019.01.040.
[58] M.A. Green, Solar cell fill factors: general graph and empirical expressions, Solid. State. Electron. 24 (8) (1981) 788–789, doi:10.1016/0038-1101(81)90062-9.
[59] M. Frazão, J. Silva, K. Lobato, J. Serra, Electroluminescence of silicon solar cells using a consumer grade digital camera, Measurement 99 (2017) 7–12, doi:10.1016/j.measurement.2016.12.017.

Ennio Luigi Comi is an energy and environmental engineer. In 2018 he has written his bachelor thesis concerning the development of a diffusion model for electrochemical impedance spectroscopy of dye-sensitized solar cells at the Institute of Computational Physics at ZHAW. Since then, his master studies are focused on model verification, experimental software validation and parameter extraction of photovoltaic devices.